# Identification of variable stages in murine pancreatic tumors by a multiparametric approach employing hyperpolarized 13C MRSI, 1H diffusivity and 1H T1 MRI

# *Identification of variable stages in murine pancreatic tumors by a multiparametric approach employing hyperpolarized $^{13}C$ MRSI, $^{1}H$ diffusivity and $^{1}H$ $T_1$ MRI*

Ricardo P. Martinho,[1&] Qingjia Bao,[1&] Stefan Markovic,[1] Dina Preise,[2] Keren Sasson,[2] Lilach Agemi,[2] Avigdor Scherz,[2] and Lucio Frydman[1,*]

*[1]Department of Chemical and Biological Physics and [2]The Moross Integrated Cancer Research Center, Weizmann Institute of Science, 7610001 Rehovot, Israel*

[&]Contributed equally to this study
[*]Email: lucio.frydman@weizmann.ac.il

**ABSTRACT**

This study explored the usefulness of multiple quantitative MRI approaches to detect pancreatic ductal adenocarcinomas (PDACs) in two murine models, PAN-02 and KPC. Methods assayed included $^{1}H$ $T_1$ and $T_2$, quantitative diffusivity maps, magnetization transfer (MT) $^{1}H$ MRI throughout the abdomen, and hyperpolarized $^{13}C$ spectroscopic imaging. The progress of the disease was followed as a function of its development; studies were also conducted for control mice in naïve state, and after subjection to mild acute pancreatitis. Customized methods developed for scanning the motion- and artifact-prone mice abdomens, allowed us to obtain quality images for these targeted regions. Contrasts between tumors and surrounding tissues, however, were significantly different. Anatomical images, $T_2$ maps and MT did not yield significant contrast unless tumors were large. By contrast tumors showed statistically lower diffusivities than their surroundings (≈8.3±0.4x$10^{-4}$ for PAN-02 and ≈10.2±0.6x$10^{-4}$ for KPC vs 13±1x$10^{-3}$ $mm^2s^{-1}$ for surroundings), longer $T_1$ relaxation times (≈1.44±0.05 for PAN-02 and ≈1.45±0.05 for KPC vs 0.95±0.10 s for surroundings), and significantly higher lactate/pyruvate ratios by hyperpolarized $^{13}C$ MR (0.53±0.2 for PAN-02 and 0.78±0.2 for KPC vs 0.11±0.04 for control and 0.31±0.04 for pancreatitis bearing mice). Although the latter could also distinguish early-stage tumors from healthy animal controls, their response was similar to that in our pancreatitis model. Still, this ambiguity could be lifted using the $^{1}H$-based reporters. If confirmed for other kinds of pancreatic tumors this means that these approaches, combined, can provide a route to an early detection of pancreatic cancer.

**SIGNIFICANCE**

This study suggests that a variety of MRI methodologies, combined, could be key aids in the early detection of PDAC and in its differentiation from other pancreatic maladies.

**RUNNING TITLE**

Multiparametric MRI characterizations on two murine pancreatic cancer models

**LENGTH**

3918 words, 5 figures, 0 tables, 53 references, one Supporting Information with 11 figures, 1 table

**Abbreviations**: ADC, Apparent Diffusion Coefficient; DWI, Diffusion Weighted Imaging; DTI, Diffusion Tensor Imaging; EPI, Echo-Planar Imaging; FLAIR, Fluid attenuated inversion recovery; MT, Magnetization Transfer; MRSI, Magnetic Resonance Spectroscopic Imaging; PDAC, Pancreatic Ductal Adenocarcinoma; RF, Radio frequency; RO, Readout; SE, Spin-Echo; SNR, Signal-to-Noise Ratio; SPEN, Spatiotemporal Encoding; TE, Echo Time; TR, Repetition Time

## 1. INTRODUCTION

Despite strides in cancer treatment, pancreatic ductal adenocarcinoma (PDAC) remains at a 5-year survival rate of 9% –a rate nearly unaffected over the last century. This makes it the fourth major cause of cancer-related deaths,[1] and it is predicted that it will become the second cause by 2030.[2] The main avenue for treatment of this cancer is resection: when possible the survival rate raises to ca. 20%.[3,4] However, 80% of patients with PDAC find out they have metastasis by the time the disease is diagnosed. This reflects PDAC's high metastatic index, coupled to a paucity of early detection methods.[5–7] Arguably, one of the reasons why the years-long induction time of PDAC goes unused treatment-wise, resides in the relative paucity of medical imaging advances to accurately characterize pancreas abnormalities.[8] Cross-sectional CT-based imaging methods are not accurate enough for the early detection of pancreatic cancer, and $^{1}$H MRI –which has unparalleled abilities to "see" soft tissues in detail– has proven remarkably ineffective when it comes to screening PDAC. One of these limitations comes from the fact that PDACs are often under-irrigated, and hence will not show hyperintensity upon injection of Gd-based contrast agents.[9,10] Standard clinical MR protocols for PDAC analyses also include $T_1$- and $T_2$-weighted imaging:[11] both $T_1$ and $T_2$ relaxation times for healthy human pancreas are known, and thus their changes could be potentially useful pathology indicators.[12] PDAC masses usually appear hypointense in fat suppressed $T_1$-weighted images when compared to healthy tissue, reflecting longer $T_1$ times associated to the fibrotic nature of the tumor.[9,13] $T_2$-weighted images by contrast show mixed intensities, leading to a weaker diagnostic usefulness.[5,14] The main MR-based procedure clinically recommended for the (relatively late-stage) diagnosis of PDAC remains Magnetic Resonance Cholangio Pancreatography (MRCP), a long-echo-time sequence that leaves solely the biliary ducts in the image, and can therefore point towards the presence of tumors if they distort the ducts' normal shapes.[15] A case has also been made for the inclusion of Diffusion Weighted Imaging (DWI) in these diagnosis;[10,16] apparently, due to the fibrotic nature of the stroma and due to the tumor's high cellularity,[17] these will have lower diffusivity and appear bright in DWI data.[16,18,19] This, however, has also been described as not always being the case for a large study of human subjects.[20] Some Diffusion Tensor Imaging (DTI) studies have demonstrated the stroma has some preferential orientation.[21] Magnetization Transfer (MT) has also been correlated with fibrosis, and has been shown in some cases as a good potential source of contrast.[17,22,23] Careful reading of the literature, however, reveals somewhat contradictory observations between different studies focusing on different contrasts; it has therefore been suggested that multiparametric explorations may be the best way to complement MRCP to target early this kind of tumors.[17,24,25]

While the aforementioned contrast sources are somehow correlated with morphological features, another relevant source of contrast may arise from metabolic markers. Although much has been done to elucidate the unique metabolic pathways underlying PDAC from their biological perspectives,[26] only few molecular imaging approaches have derived from these and translated onto a clinical setting. The archetypical metabolic imaging reporter of cancer is FDG-PET,[27] which derives its strength from the enhanced glycolysis underlying the Warburg Effect.[28] FDG-PET, however, has not become for PDAC as common a tool of diagnosis as for other tumors, most likely due to the organ's perfusion properties.[6] MR also offers a number of routes to study metabolic alterations, foremost among them by resorting to hyperpolarized $^{13}$C-labeled substrates.[29,30] The promise of this procedure lies in using magnetic resonance to examine the conversion of a metabolite that like $^{13}C_1$-pyruvate is involved in glycolysis, and monitor its transformation to $^{13}C_1$-lactate thanks to the orders-of-magnitude enhancements afforded by hyperpolarization. The spectral dimension of this experiment allows one to quantify the ratio of these individual metabolic peaks throughout an organ as a function of time, thereby potentially enabling the detection of tumors. While the orthogonal spatial dimensions of the ensuing MR spectroscopic imaging (MRSI) experiment can map these changes onto specific organ regions. This approach has been employed to target certain pancreatic animal models, where metabolic fluxes promised to diagnose the success or failure of a treatment.[32,34] Preliminary hyperpolarized $^{13}$C MRSI measurements also showed evidence of highlighting diseased tissues, including in a clinical setting.[32]

This work reports on our experience looking for PDAC MR markers that combine all the above-mentioned $^{1}H$ and $^{13}C$ experiments, in a search for a reliable multiparametric approach capable of revealing the onset of these tumors. The focus was on two PDAC models: PAN-02, an immortalized mouse-derived cell line leading to orthotopic PDAC when injected on conventional black mice pancreases; and KPC, a programmed model possessing key similarities with human PDACs.[34,35] PAN-02 is a well-established Grade III adenocarcinoma model developed by chemical induction with 3-methylcholanthrene in male C57BL/6 mice,[36] containing a loss of function mutation in the SMAD4 gene that is functionally similar to inactivating mutations in approximately 30% of human pancreatic cancers. PAN-02 also has a dense desmoplastic stroma that characteristic of "cold" tumors, which could be particularly relevant for evaluation of MRI techniques that, like DWI or MT, could be affected by significant stromal changes. KPC differs from PAN-02 in that it is a more slowly growing tumor, that recapitulates many human pancreatic cancer features –including immune defects associated with a lack of high-quality effector cells, barriers to effector cell infiltration, and immune checkpoint signaling;[37] this has made KPC a particularly useful model for studying the genetic mechanisms of PDAC carcinogenesis, and as preferred model for drug discovery purposes.

In this work, morphological and contrast inputs were sought from a combination of $^{1}H$ MRI techniques –$T_1$ and $T_2$ mapping, ADCs, MT mapping– together with $^{13}C$-based hyperpolarized imaging approaches. Emphasis was placed on analyzing these outcomes in a systematic longitudinal fashion, and on distinguishing their responses from pancreatitis cases. A significant challenge in these experiments stemmed from the fact that mice pancreases are significantly smaller than those of humans: this rendered their systematic identification quite challenging.[38] Thus we opted for studying the contrast between the emerging pancreatic tumor and surrounding tissues, under the assumption that these will present general similarities with human abdominal regions. These tests were successful at identifying some leads that highlighted the tumors at early stages, even if with ambiguity against mice pancreatitis models. If further validated, it appears that the combination of some of the assayed approaches could prove useful for translation into clinical settings.

## 2. MATERIALS AND METHODS

***Animal models.*** Animal experiments were preapproved by the Weizmann Institute's IACUC, which is fully accredited by the AAALAC, the US NIH Office of Laboratory Animal Welfare and the Israel Ministry of Health. Eight male black mice were used in the PAN-02 orthotopic tumor studies, ten were used in the KPC counterparts, and an additional five in the pancreatitis studies. Four black mice were scanned for control purposes: two of these naïve, and two after injection of Matrigel® (the tumor cell carrier). Mice were scanned longitudinally (every five days) to investigate the progress of disease, over the course of a four-week period. Due to their slow growth we decided to spare KPC-implanted from an early stage scanning by hyperpolarized $^{13}C$ MRSI, as these would have resulted in multiple injections leading to a high animal mortality; hyperpolarized $^{13}C$ MRSI results were thus only collected one month post-implantation.

*Orthotopic tumor implantation – PAN-02.* The protocol used in this study is based on that described by Jiang *et al*.[39] PAN-02 cells were cultured in RPMI growth medium containing 10% FBS, 2mM glutamine, 100µg/ml penicillin and 100U/ml streptomycin. The mice were anesthetized, shaven and cleaned with a 10% povidone solution. For the implantation, an ~1.5cm incision was made through the skin and underlying abdominal muscle left laterally from the mid-line. The spleen was gently pulled out of the abdomen exposing the pancreas. PAN-02 tumor cells (20,000) admixed with Matrigel® (Corning) in 0.05 mL PBS were injected into the pancreas using a 29G insulin syringe. The needle was held in place for 10sec after injection to allow Matrigel solidification and prevent leakage. The musculature and the skin were closed using 4-0 nylon sutures. Mice were kept on a heating plate until recovery from anesthesia.

*Orthotopic tumor implantation – KPC*. The KPC-Luc-mCherry line was received from Prof. David Tuneson (Cold Spring Harbor Laboratory), who also shared the implantation protocol we followed. Mice were anesthetized by ketamine/xylazine and, after being subject to analgesic agents

(s.c. 0.05 mg/kg of buprenorphine), they were subject to a laparotomy (5-10 mm) over the left upper quadrant of their abdomen to expose the peritoneal cavity. The pancreas was exteriorized onto a sterile field, and KPC tumor cells ($2\times10^4$ cells suspended in 20 ml of sterile PBS mixed with 20 ml Matrigel) were injected into it via a 30-gauge needle. Successful injection was confirmed by the formation of a liquid bleb at the site of injection. The pancreas was then gently placed back into the peritoneal cavity, and the peritoneum and skin were closed back with a suture and autoclips, respectively. Mice were subsequently placed on a heating pad, moved back into the cage and monitored until recovery from anesthesia.

Both PAN-02 and KPC implanted animals were euthanized after scanning. Their pancreases were excised for histology with H&E and Maison staining, and sent to Pathovet (Israel) for analysis. Supporting Information Table S1 provides the main characteristics revealed from such studies.

*Pancreatitis induction* A protocol leading to mild acute pancreatitis symptoms – acute as opposed to chronic, and mild as there were not severe symptoms– was adopted from V. Krizhanovsky's lab (Weizmann Institute) for comparing against the tumor analyses. The model is based on the procedure of Carriere *et al*:[40] Caerulein (Sigma, St. Louis MO) was diluted in 6% Dextran 70 and 0.9% NaCl, and injected at a dose of 50 ug/kg of body weight. Mice were subjected to a series of seven hourly intra-peritoneal injections of caerulein, that were repeated 48hr later. As controls, two mice also received vehicle injections. Imaging was performed during 3 days after the second series of injections; following the MR scans the animals were euthanized, and their pancreases excised for histology with H&E and Maison staining.

***MRI Protocols.*** For their scanning, animals were placed under anesthesia with isoflurane (1 – 2%) via a vaporizer, and their body temperatures were kept constant using a water-based heating system. Respiration was monitored via a pressure sensor (SA – II, Stony Brook, NY) and maintained at 30 – 50 breaths per minute. All the images were reconstructed and analyzed employing custom Matlab code. Quantitative analyses were based on ROIs defined to cover the whole tumor region; representative surrounding ROIs were taken when necessary in the proton imaging studies. The animals were followed through using an array of $^1$H MRI and hyperpolarized $^{13}$C MRSI methods.

*Proton Imaging.* $^1$H MRI data were collected on an Agilent DD2® 7T/110mm bore horizontal magnet scanner (Santa Clara, CA) equipped with a 100 G/cm maximum gradient triple-axis setup, using a quadrature 40 mm volume (Millipede) coil. Respiratory triggering was employed to ensure that motion artifacts were minimized. Multiple contrast sources were explored employing manufacturer provided sequences for $T_2$-weighted (Fast-spin-echo FSE, also known as RARE) and $T_1$ (Fluid attenuated inversion recovery, FLAIR). MT was probed using an in-house modified RARE sequence. VNMRJ-based EPI and homebuilt SPatiotemporal ENcoding (SPEN) sequences were written and assayed for DWI;[41,42] a multi-spin-echo SPEN sequence was also written for fast $T_2$ mapping,[43] as this allowed us to compensate for inhomogeneities and motion artifacts in the abdominal region. These SPEN-based sequences are available upon request or from https://www.weizmann.ac.il/chemphys/Frydman_group/software, as are the corresponding processing macros. All experiments were performed employing a fat saturation module, based on a 90° set at approximately 1.4 ppm (in the TMS scale) followed by a crusher gradient.

*Diffusion weighted imaging.* DWI and ADC mapping are challenging procedures when targeting the abdominal region housing the pancreas, susceptible as it is to motions, fat/water interferences and field inhomogeneities.[44] This is particularly true when methods that require fast imaging –such as the SE EPI protocol usually underlying DWI– are used to target what may be small diffusivity differences in the abdomen of living mice. To overcome these obstacles, we relied on SPEN MRI for imaging diffusivities in the implanted animals. SPEN is a single-shot imaging approach[45] that, as discussed in more detail in Ref. 42, is much less influenced by these factors and challenges. This is further demonstrated in Supporting Figure S1, showing images collected on a mouse that developed a clearly discernible PAN-02 tumor. The SPEN-based DWI protocol used consisted on acquiring 4 slices with an effective TE=40 ms, TR =1.5-2.0 s, slice thickness=1 mm, and in-plane resolution of 200-250 μm; each data included interleaving 5 shots and 2 averages.[42] DWI was attained by using a bipolar-gradient

pulse module with $\delta$ = 4.0 ms, $\Delta$ = 8.5 ms, diffusion gradient = 38 G/cm, three orthogonal diffusion directions (b-weighting = 1200 s/mm$^2$). The use of a single, high b-value for determining the ADC of the tumors and surrounding tissues is justified in Supporting Fig. S11, which shows that b-values of 800 and 1200 s/mm$^2$ yield identical ADC maps, and similar diffusion weighted images.

*FLAIR-based $T_1$ mapping.* The general protocol for $T_1$ mapping was based on a FLAIR method employing a scanner-provided sequence, with 6 to 8 inversion times spread between 0.05 and 1.45 s (0.05, 0.25, 0.45, 0.65, 0.85, 1.05, 1.25, 1.45 s). Images were collected with RARE using an acceleration factor = 8, TE = 8 ms, TR = 6 s, a two-slice acquisition with an in-plane resolution of 200-250 µm, and a slice thickness of 1 mm with 0.1 mm gap.

*Hyperpolarized $^{13}C$ imaging.* For the hyperpolarized $^{13}C$ experiments, $^{1}H$ MRI and $^{13}C$ MRSI images were recorded on a 1987 Bruker Biospec 4.7T/400mm bore horizontal scanner. These data were recorded using a $^{1}H/^{13}C$ double-resonance, whole-body 40mm diameter volume coil (Doty Scientific, Columbia, SC). $^{13}C$ MRSI images were acquired using a centric chemical-shift imaging sequence[46] with differential excitation angles = 25˚ (on lactate) and 5˚ (on pyruvate), slice thickness = 0.4-0.7 cm, in-plane matrix size = 8x8, and square 35x35 mm$^2$ (for axial slices, which therefore only focused on the abdomen) or 40x40 mm$^2$ (for sagittal slices) FOVs. Spectral domains were sampled with 384 complex data points and a 119 ppm bandwidth (64ms acquisition time, TR=68 ms), resulting in overall measurement times of 3 sec per image. $^{13}C$ images were processed using custom-written Matlab® routines including weighting and zero filling, leading to 32x32 in-plane and 512 spectral elements. Ancillary $^{1}H$ anatomical images were recorded before the hyperpolarized agent injection using a gated FLASH imaging sequence, targeting a 40x40 mm$^2$ square FOV, with TE=6.3 ms and TR=615 ms, or with a RARE sequence with a 40x40 mm$^2$ square FOV, 4 echoes, TE=30 ms and TR=5000 ms (RARE images highlighted somewhat better the large tumors than FLASH). The metabolic agent assayed was $^{13}C_1$-labeled pyruvic acid, which was polarized as a neat liquid after preparing a 15mM radical solution containing the Trityl (Ox63) radical, in an Oxford Instruments Hypersense® device operating at 94 GHz and 1.4K. After polarizing for ca. 60 min the frozen pyruvic acid pellet was dissolved with a buffer of 60 mM NaOH, 40 mM, Trizma-PreSet (pH=7.6), EDTA 0.1 g/L and 0.9% NaCl, and a 0.5 ml bolus of the resulting 37 ˚C, pH 7.5, 80 mM hyperpolarized $^{13}C_1$ pyruvate solution was injected into the mouse tail-vein. $^{13}C$ acquisitions were performed as detailed above, starting 25 sec after this injection and repeated every 3 seconds. Although ca. 10 2D MRSI data sets were collected in this manner, the $^{13}C$ signals had usually decayed into the noise after the first two-three acquisitions. Hence no kinetic analysis was implemented: the hyperpolarized data shown represent the average of the two data sets collected with highest signal, thus representing the metabolic status ≈30 sec past the bolus's injection.

## RESULTS

All mice bearing PDAC tumors –those based on PAN-02 and those based on KPC– were scanned longitudinally and compared to one another. In the PAN-02 model tumors grew relatively slowly, and could barely be identified by anatomical $^{1}H$ MRI ca. 10 days post-implantation; the KPC model growth was even slower, and tumors could only be identified through $^{1}H$ MRI after ca. 22 days post-implantation. Hence, we refer to these periods as "the early-detection" stage. Tumors in this stage ranged from ~1 to 3 mm in diameter, whereas late stage tumors had ca. 8-10 mm diameters. Different $^{1}H$ MR contrasts were explored throughout this and later periods. Contrast sources that had been tried before include T2 and MT weighting and mapping, respectively.[14,17,22,23] Figure 1 illustrates representative data obtained when assaying these two parameters on animals bearing large PAN-02 tumors. As can be appreciated from these data, neither of these approaches facilitates the tumor identification even weeks following implantation, when they had already reached ≈1cm and become clearly visible in the anatomical image. Indeed, there is an MT effect present in these tumors (Fig. 1A), but it is not sufficiently different from the response of the surrounding issue, to be considered as providing an added value –not even when tumors are this large. Likewise, the values of the tumor's

transverse relaxation times $T_2$ are very similar to those of the other tissues in the abdominal region (Fig. 1B), explaining why $T_2$-weighted imaging is usually insufficient for tumor identification.

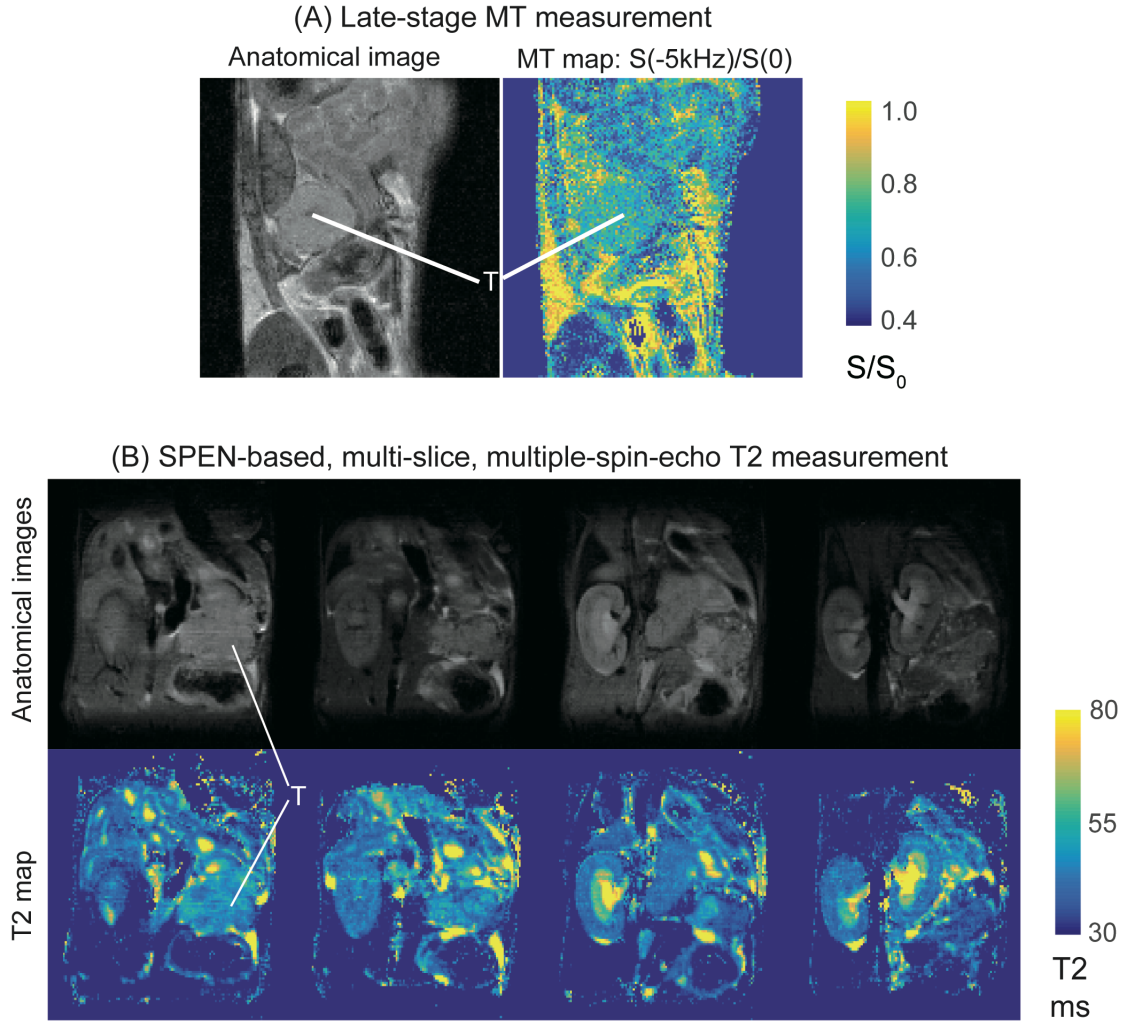


***Figure 1.*** Representative MT (A) and $T_2$ (B) maps collected for animals possessing late-stage PAN-02 tumors (marked by Ts): notice that these tumors are large enough to show in the anatomical images. MT maps were collected using a RARE detection module with RARE factor = 8, TE = 8 ms, TR = 4 s for a two-slice acquisition with an in-plane resolution of 200-250 μm and slice thickness of 1 mm, with a gap of 0.1 mm. They used 300 ms long presaturation pulses with 5.8 μT, stepped over 15 points in 5 kHz increments; they are here shown as S(-5 kHz)/S(0), as this is representative of the MT curve (whose response was ~20 kHz wide). $T_2$ maps were collected using a multi-echo SPEN sequence,[43] for the sake of speeding up the acquisition, while preventing motion-derived and other artifacts. This involved the acquisition of 5 echoes separated by TE=26 ms times. Other parameters: TR =2.0 s, slice thickness=1 mm, in-plane resolution of 200-250 μm, 5 interleaved, shots and 8 averages per shot, 4 slices with a 0.1 mm gap.

It has been argued that diffusivity parameters arising either as contrasted regions in DWI experiments or as abnormally low ADCs in the corresponding maps, might be more promising approaches for PDAC identification.[16] Figure 2A illustrates an example on the use of SPEN-based diffusivity measurements, this time for the detection of early-stage PDAC tumors, ≈2 mm in diameter.

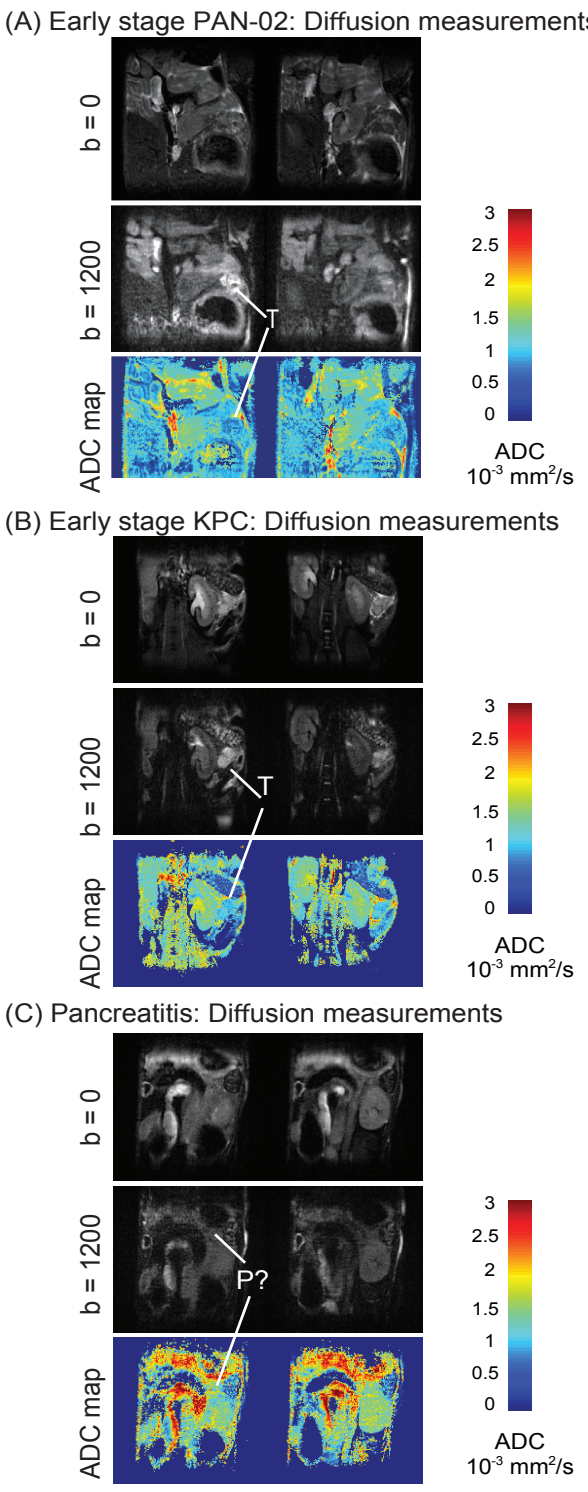


***Figure 2.*** Demonstrating the contrast attained by SPEN-based diffusion monitoring experiments to detect early stage tumors. (A) Exam on an animal performed 8 days post-implantation, when the PAN-02 tumor has reached a diameter of only ≈2 mm. (B) Idem for a mouse implanted with KPC tumor 19 days post-implantation, when the tumor has reached a diameter of only ≈2 mm. (C) Idem but for a mouse that had been exposed to a caerulein treatment leading to pancreatitis symptoms, 24 hs prior to the exam. Details on the experimental protocol are provided in the Materials and Methods section.

DWI data clearly highlights the tumors in the b-weighted data, under conditions that barely highlight any other abdominal region. This is valid for both types of tumor models employed in this study. The origin of this contrast can be further quantified from ADC maps that provide slow isotropic diffusivity values of ≈$8\times10^{-4}$ $mm^2s^{-1}$ and ≈$10\times10^{-4}$ $mm^2s^{-1}$ for the PAN-02 and KPC tumors respectively, compared to surrounding values of ≈$13\times10^{-4}$ $mm^2s^{-1}$. This difference in water diffusivity vs the surrounding tissues, presumably reflects the higher cellularity of the tumorous mass; the slight differences observed between the two tumor models' ADCs can be attributed to their microscopic distinctions. Similar good contrasts could be observed for other mice and for larger, later-stage PAN-02 and KPC tumors, as illustrated in the Supporting Information (Figures S2 and S3). It is interesting and relevant to compare this behavior against that arising upon examining an animal on which pancreatitis had been chemically induced by the injection of caerulein: these did not reveal any slow-diffusing tissue that could be related to such external procedure (Figure 2B).

As mentioned, another source of PDAC contrast has been postulated for $T_1$ weighting. Recent literature indicates that heightened $T_1$ relaxation values can be observed in human patients, with lesioned tissues having $T_1$ ≈1.7 s at 3 T.[47] This was here explored using a FLAIR sequence, which we applied to mice bearing PAN-02 and KPC tumors, as well as to pancreatitis controls. $T_1$ weighted images showed a hypointense region associated with tumors of sufficient size, which is relatively hard to identify given the heterogeneity of the region in question. Tumors could be better defined by quantitative mapping of their $T_1$ values (Figure 3A and 3B), as these led to slightly longer values (≈1.45±0.05 s for both KPC and PAN-02 models) than most of the surrounding tissues in the abdominal region (0.95±0.10 s). These values are in correspondence with the aforementioned human PDAC results. By contrast, identical assays performed in mild acute pancreatitis-bearing mice, did not provide any meaningful contrast in the $^1H$ $T_1$ experiments (Figure 3C). A low pancreas T1 value for pancreatitis-bearing mice has also been described before.[47,48] Hence, overall, this also appears as a promising

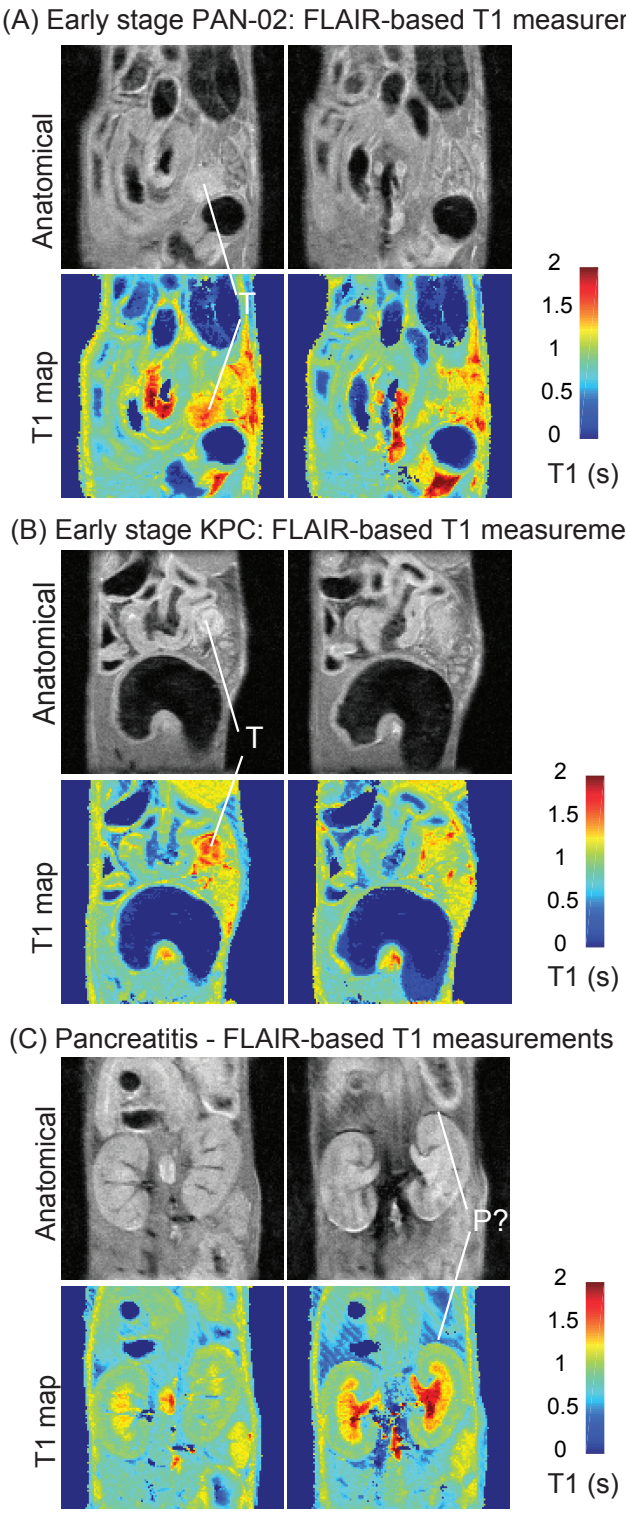


***Figure 3.*** Demonstrating the contrast attained by T1 FLAIR experiments for early stage tumors. (A) Two slices collected for an animal 8 days post PAN-02 implantation. Notice the slight hypointensity and longer $T_1$ values characteristic of the forming tumor. (B) Idem for a mouse implanted with KPC tumor 17 days post-implantation, when the tumor has reached a diameter of ≈1.5 mm. (C) Idem for a mouse exposed to caerulein treatment to mimic pancreatitis. Details on the acquisition protocols are provided in the Materials and Methods section.

early-stage diagnosis contrast. As summarized in the Supporting Figures S4 and S5, this $T_1$ contrast was also retained through later stages of the tumor's development. Still, tumor progression also evidences an increase in the heterogeneities characterizing the $^1$H observables ($T_1$, ADC) with tumor size – even if the average values for these observables remain fairly constant with tumor size (Supporting Information, Fig. S6).

As complement to these *in vivo* $^1$H results, a series of studies were collected *in vitro* on surgically extracted PAN-02 tumors (Supporting Fig. S7A). These results recapitulated only partially the *in vivo* observations. The ADC values measured under such conditions were lower than those *in vivo,* a feature which has also been reported in previous studies (Supporting Fig. S7B).[49,50] These measurements also indicated a marked kurtosis –a deviation from unrestricted diffusivity– which could be related to the dense, locally ordered morphology revealed for the tumorous stroma by staining and microscopy (Supporting Figs. S7A, S7C). MT measurements repeated *ex vivo* once again failed to highlight contrast between even large tumors and the pancreas –an organ which by contrast to the *in vivo* measurements, could now be clearly discerned in the MR image (Supporting Fig. S7D).

In addition to these $^1$H measurements, MR's competence to detect PDAC tumors was assayed by injection of hyperpolarized $^{13}C_1$-pyruvate. As mentioned, hyperpolarized $^{13}$C MRSI has already been tested as potential reporter of a pancreatic cancer model with promising results;[31] here our focus was on exploring whether it could also highlight the PAN-02 and KPC models at both early- and late-stages and, if so, its ability to differentiate these tumors from pancreatitis abnormalities. The reporter in this kind

of experiments is the anaerobic glycolysis enhancement brought about by the disease, presumably reflecting the Warburg effect. This can then be tracked either by comparisons on how the kinetics of the pyruvate→lactate transport and conversion are affected in different regions, or by mapping the ratios between the pyruvate and lactate peak intensities at a properly-chosen, single timepoint. The rapid consumption of the hyperpolarization in the analyzed cases, leading to a decay of the images' $^{13}C$ signals into noise levels after two or three repetitions, led us to adopt the latter of these representations: two spectrally-resolved $^{13}C$ images arising ca. 30 sec post-injection, were thus coadded and their relative pyruvate and lactate spectral intensities evaluated. Figure 4 presents such results for five prototypical cases involving a healthy animal control (injected just with gelling medium), an animal for which the PAN-02 tumor is growing but which is still invisible in the $^{1}H$ anatomical image (early-stage detection), animals for which KPC and PAN-02 tumors are already clearly discernible by $^{1}H$ MRI (late-stage detection), and an animal that has been treated to develop pancreatitis. As, despite the nuclear hyperpolarization, sensitivity in these $^{13}C$ metabolic MRSI experiments was still limited, these images are presented in all cases superimposed on $^{1}H$ MRIs of the same regions collected at higher spatial resolutions. The naïve controls show similar distributions for the pyruvate and lactate, concentrating more or less close to the kidney with a ca. 10-fold intensity ratio. By contrast both early- and late-stage tumors clearly identify much higher lactate/pyruvate ratios, which are magnified by ca. 3x in the early-stage cases, and by ca. 5x in late-stage instances. In the latter instances the tumors are clearly visible on the $^{1}H$ images and the most intense lactate signals originate from these masses' approximate centers. By contrast, for the early-stage cases the $^{1}H$ images do not identify the contours of the tumor, and hence the origin of the maximal $^{13}C$-lactate signal intensities cannot be anatomically correlated. It is however reasonable to assume that it corresponds to the tumor's putative location. The response of hyperpolarized $^{13}C$ MRSI to the pancreatitis model was also investigated. This time, and by contrast to the $^{1}H$ $T_1$ and ADC measurements that had not observed any differences between inflamed and healthy tissues, in the $^{13}C$ MRSI also the pancreatitis models led to a ca. three-fold increase in the Lac/Pyr ratio, when compared against ratios arising from other abdominal regions or from controls. Additional representative examples collected on other animals and as a function of disease progression, tumor type and image processing conditions, are presented in the Supporting Information (Figs. S8 - S10).

A quantitative analysis of the various methods' capacity to reveal early- and late-stage tumors for the whole cohort of animals studied, is given in Figure 5. The highest contrast to PDAC on the mice studied, arose on the basis of $^{13}C$-lactate/$^{13}C$-pyruvate ratios (Fig. 5A); this contrast could also distinguish between early- and late-stages, at least for the PAN-02 case, and is hence noted in the Figure. By contrast no such distinction could be found between early- and late-stages in the $^{1}H$-derived parameters, as neither ADC (Fig. 5B) nor $T_1$ (Fig. 5C) showed significant changes with the size of the tumor (Supporting Information, Fig. S6). Interestingly both of the tumor models demonstrated identical longitudinal relaxation values whereas KPC showed a slightly higher ADC value than that of PAN-02 –even if still smaller than that of their respective surroundings. Furthermore, MTC data measured longitudinally for the KPC cohort showed no clear contrast between tumor and surrounding tissue (Fig. 5D). A characteristic of the $^{13}C$ measurements was that, despite their high sensitivity, they lacked certain specificity needed to distinguish our early-stage PDACs from our pancreatitis models. This is further illustrated in Fig. 5E, which summarizes ROC analyses for these cohorts based on the hyperpolarized data.

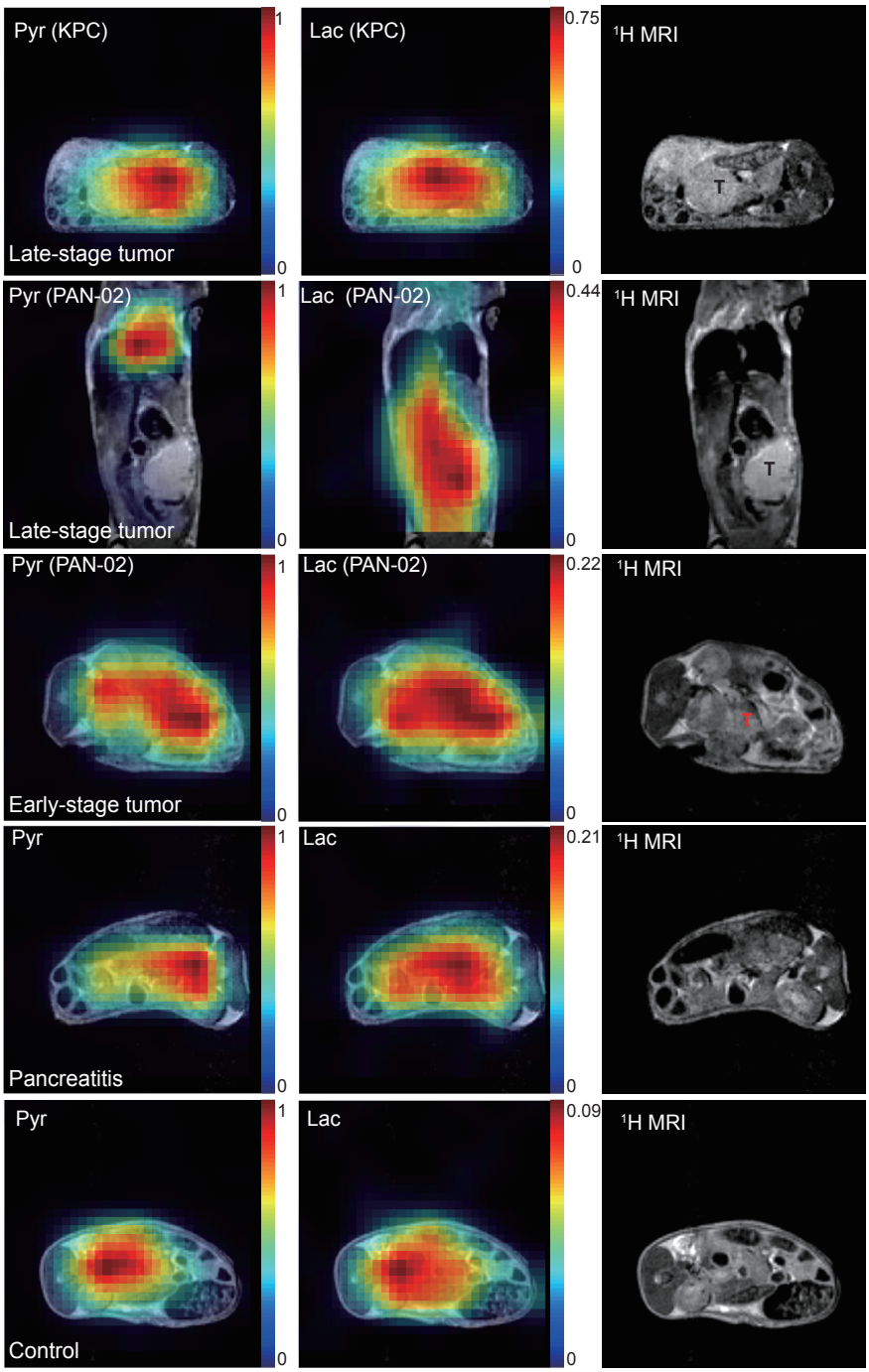


**Figure 4.** Representative metabolic maps arising from the tail-vein injection of a 0.5 ml bolus of 80 mM hyperpolarized $^{13}C_1$-pyruvate on different abdominal mice regions, illustrated in color and placed on top of grayscale anatomical $^{1}H$ images recorded at 4.7 T. The $^{13}C$ MRSI data shown was collected 25 sec after the injection, and images associated with the hyperpolarized pyruvate and lactate peaks, are shown on the left and middle columns respectively. For clarity the anatomical $^{1}H$ images are also reproduced by themselves on the right-hand column, with "T" indicating the approximate tumor's position (in the early-stage case, as presumed from the surgical implantation). First row: full grown, late-stage KPC tumor case. Second row: same, for a PAN-02 tumor. Third row: small, early-case PAN-02 tumor. Fourth row: pancreatitis model case. Fifth row: wildtype control. For each row, all colormap bars were scaled between 0 and 1 –the latter denoting the maximum $^{13}C$-pyruvate signal throughout the image. All these $^{13}C$ MRSI data are shown after zero-filling the collected data to 32x32 matrices; Fourier analyses of the same data without zero-filling are shown in Supporting Figure S10. Further details on the experimental protocol are provided in the Materials and Methods section.

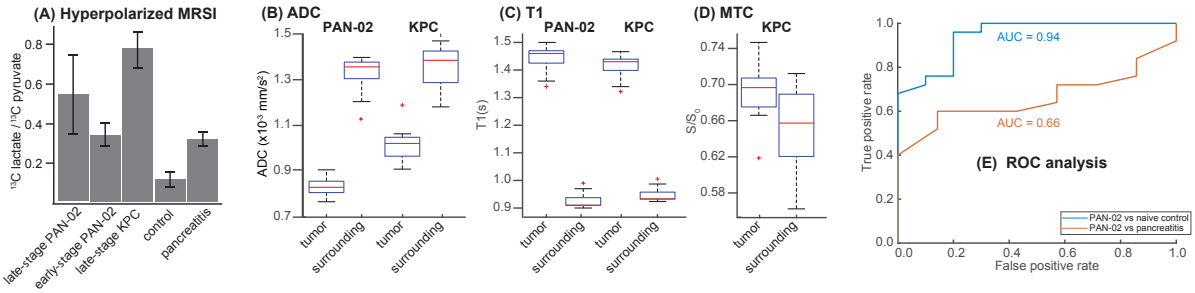


***Figure 5.*** (A-D) Summary and statistical analysis of the quantitative data obtained through the different sources of contrast followed longitudinally along PDAC tumor progression. The $^{13}$C lactate/$^{13}$C pyruvate ratios were obtained from hyperpolarized $^{13}$C studies in mice with PDAC tumors (PAN-02 and KPC), naïve animals, and pancreatitis-bearing mice. Apparent Diffusion Coefficients (ADCs), spin-lattice relaxation times $T_1$ and MTC values were obtained from the tumor and surroundings. As in these latter cases pancreatitis could not be clearly identified in the $^1$H maps, these data were not included in this analysis: their values were thus akin to those of their surroundings. Furthermore, as the behavior displayed by the $^1$H ADC,T1 and MTC observables was more or less constant throughout tumor progression, no distinction was made between early and late stages in (B), (C) and (D). (E) Receiver Operating Curve (ROC) analysis for the hyperpolarization-based metabolic imaging data. This Matlab-based analysis was performed employing a logistic regression considering the PAN-02 tumor $^{13}$C-lactate/$^{13}$C-pyruvate peak ratios as measures of "positives" and ratios of pancreatitis and naive controls as "negatives". AUC represents the area under the resulting curves.

## DISCUSSION & CONCLUSIONS

This study explored, longitudinally, multiple complementary magnetic resonance approaches as potential tools for the characterization of PDAC and its distinction of pancreatitis. For assessing these mice-based models, PAN-02 and KPC tumor implantations and caerulein-induced inflammation procedures were adopted, and implemented on immunocompetent animals. $T_2$, MT, DWI, $T_1$ of $^1$Hs as well as hyperpolarized $^{13}$C metabolic imaging were assayed in these MR mapping trials. This identified three main viable sources of tumor contrast, associated with DWI, $T_1$ mapping, and mapping the $^{13}$C lactate/pyruvate ratios. The sensitivity with which these parameters reported the malignancy, particularly for the early tumor development stages, varied: $T_1$ mapping had the lowest highlighting contrast; its lengthening by ca. 50% in the tumorous region, however, being in line with recently reported human measurements.[47] The contrast attained via diffusion weighting had been explored in a number of clinical setting,[18-21,47] and the results are conflicting. Whereas earlier studies confirmed a reduced diffusivity in the tumor area,[18-21] a recent report measured average ADCs of $1.5\text{x}10^{-3}$ mm$^2$/s for PDAC –higher than ADCs for normal control pancreas.[47] While the types of tumors and tissues will naturally be different, the results here obtained for the various mice models suggest a reduction in the average ADC for the tumor regions. The b-values used in our DWI studies were slightly higher than those normally used in clinical settings, but could be translated to human scanning given a modest increase in signal averaging times. The measurements performed in extracted tumors also providedinsight a kurtosis effect, that was observed at long diffusion times (Supporting Fig. S7). Kartalis *et al*[51] have reported a similar effect for humans, that could also be exploited to increase the diagnostic accuracy of PDAC patients. Additional sources of contrast like MT, which had been identified as promising sources for other PDAC models,[17,22,23] failed to highlight the tumors in our PAN-02 or KPC cases. Likewise $T_2$s, whose contrast is known from clinical examinations to be low for human PDAC, were of low diagnostic value also in our PDAC models. $^{13}$C hyperpolarization had the largest of the PDAC contrasts here assessed, and although with limited spatial resolution the behavior displayed by the Lactate/Pyruvate ratio was clearly different from the control measurements for both PDAC models. This was not *a priori* a given since, as mentioned, perfusion in PDACs is normally assumed to be poor. On the other hand, both the model of Serrao et al[31] as well as the results arising for the PAN-02 and KPC implants, clearly indicate that $^{13}C_1$-pyruvate reaches the tumors and gets metabolized before its hyperpolarization had a chance to decay. Despite this valuable promise an ambiguity remained concerning hyperpolarized $^{13}$C MRSI's ability to distinguish tumors from pancreatitis; this could reflect the known fact that certain inflammations can also increase the rate of

glycolysis.[52,53] It remains to be seen if a similar ambiguity arises in human cases. Such early-stage cases were not visible in the ancillary anatomical $^{1}$H images that were collected together with the hyperpolarized studies, as the lower field (and much older scanner) used in this study prevented us from obtaining quality *in situ* ADC and $T_1$ maps. However, based on the different ADCs and $^{1}$H T1s that at 7T we could observe between the tumors and pancreatitis / healthy tissues, it appears that by combining all these reporters a differential, more reliable early-stage PDAC vs pancreatitis diagnosis could be possible. The hyperpolarized studies also suffer from limited spatial resolution that could pinpoint the location of a tumor, yet this could also eventually become available from the ancillary ADC and $T_1$ $^{1}$H measurements, whose contrasts would then become diagnostically more reliable as the tumor development progresses. It remains to be seen if $T_1$ measurements done at other clinically-relevant fields or if utilizing different reporters, could help distinguish the lactate/pyruvate ambiguity arising for the early-stage/pancreatitis scenarios. This is currently under investigation.

In conclusion, a comprehensive multimodal protocol exploring multiple contrast sources was investigated in the hope of achieving early PDAC detection in two different mice models which are comparable to PDAC cases present in humans; differences against pancreatitis were also sought. Three potentially translatable contrast sources were identified: SPEN-based DWI and ADC mapping, $T_1$ mapping via Inversion Recovery, and hyperpolarized $^{13}$C MRSI. Findings from these methods could jointly reveal the presence of PDAC even at an early stage, when the tumor is small and treatable yet undetectable by anatomical $^{1}$H images. Proton imaging studies highlighted significant differences with the pancreatitis model – thus demonstrating a potential specificity if suitably combined with the hyperpolarized $^{13}$C data. These studies need to be further refined, but open promising routes towards treatment monitoring and the goal of eventually translating them into a clinical setting.

**Acknowledgments**

The authors are grateful to Dr. Ori Brenner (Weizmann's Veterinary Services) for his technical assistance and valuable discussions. This work was supported by the Kimmel Institute for Magnetic Resonance (Weizmann Institute), the Israel Science Foundation (grants 2508/17 and 965/18), a Thompson Family Foundation grant, and the EU Horizon 2020 programme (Marie Sklodowska-Curie Grant 642773).

**References**

(1) Siegel, R. L.; Miller, K. D.; Jemal, A. Cancer statistics, 2019. *CA. Cancer J. Clin.* **2019**, *69* (1), 7–34.

(2) Rahib, L.; Smith, B. D.; Aizenberg, R.; Rosenzweig, A. B.; Fleshman, J. M.; Matrisian, L. M. Projecting cancer incidence and deaths to 2030: The unexpected burden of thyroid, liver, and pancreas cancers in the united states. *Cancer Res.* **2014**, *74* (11), 2913–2921.

(3) Bilici, A. Prognostic factors related with survival in patients with pancreatic adenocarcinoma. *World J. Gastroenterol.* **2014**, *20* (31), 10802–10812.

(4) Poruk, K. E.; Firpo, M. A.; Adler, D. G.; Mulvihill, S. J. Screening for pancreatic cancer: Why, how, and who? *Ann. Surg.* **2013**, *257* (1), 17–26.

(5) Lee, E. S.; Lee, J. M. Imaging diagnosis of pancreatic cancer: A state-of-the-art review. *World J. Gastroenterol.* **2014**, *20* (24), 7864–7877.

(6) Zhang, L.; Sanagapalli, S.; Stoita, A. Challenges in diagnosis of pancreatic cancer. *World J Gastroenterol May World J Gastroenterol* **2018**, *21* (2419), 2047–2060.

(7) Yin, T.; Liu, Y.; Peeters, R.; Feng, Y.; Ni, Y. Pancreatic imaging: Current status of clinical practices and small animal studies. *World J. Methodol.* **2017**, *7* (3), 101–107.

(8) Brentnall, T. A. Progress in the Earlier Detection of Pancreatic Cancer. *J. Clin. Oncol.* **2016**, *34* (17), 1973–1974.

(9) Miller, F. H.; Rini, N. J.; Keppke, A. L. MRI of adenocarcinoma of the pancreas. *AJR. Am. J. Roentgenol.* **2006**, *187* (4), 365–374.

(10) Jha, P.; Yeh, B. M.; Zagoria, R.; Collisson, E.; Wang, Z. J. The Role of MR Imaging in Pancreatic Cancer. *Magn. Reson. Imaging Clin. N. Am.* **2018**.

(11) Schima, W.; Ba-Ssalamah, A.; Goetzinger, P.; Scharitzer, M.; Koelblinger, C. State-of-the-art magnetic resonance imaging of pancreatic cancer. *Top. Magn. Reson. Imaging* **2007**, *18* (6), 421–429.

(12) Damen, M.; van Leeuwen, M.; Webb, A.; Klomp, D.; de Castro, C. A. Measurement of T1 and T2 relaxation times of the pancreas at 7 T using a multi-transmit system. *Magn. Reson. Mater. Physics, Biol. Med.* **2019**, No 0123456789.

(13) Obuz, F.; Dicle, O.; Çoker, A.; Sağol, Ö.; Karademir, S. Pancreatic adenocarcinoma: Detection and staging with dynamic MR imaging. *Eur. J. Radiol.* **2001**, *38* (2), 146–150.

(14) Tamm, E. P. Imaging of pancreatic ductal adenocarcinoma: State of the art. *World J. Radiol.* **2013**, *5* (3), 98.

(15) Prasad, S. R.; Sahani, D.; Saini, S. Clinical Applications of Magnetic Resonance Cholangiopancreatography. *J. Clin. Gastroenterol.* **2001**, *33* (5), 362–366.

(16) Nissan, N. Modifications of pancreatic diffusion MRI by tissue characteristics: what are we weighting for? *NMR Biomed.* **2017**, *30* (8), 1–11.

(17) Farr, N.; Wang, Y.-N.; D'Andrea, S.; Gravelle, K. M.; Hwang, J. H.; Lee, D. Noninvasive characterization of pancreatic tumor mouse models using magnetic resonance imaging. *Cancer Med.* **2017**, *6* (5), 1082–1090.

(18) Sandrasegaran, K.; Nutakki, K.; Tahir, B.; Dhanabal, A.; Tann, M.; Cote, G. A. Use of diffusion-weighted MRI to differentiate chronic pancreatitis from pancreatic cancer. *Am. J. Roentgenol.* **2013**, *201* (5), 1002–1008.

(19) Tang, M.-Y.; Zhang, X.-M.; Chen, T.-W.; Huang, X.-H. Various diffusion magnetic resonance imaging techniques for pancreatic cancer. *World J. Radiol.* **2015**, *7* (12), 424.

(20) Fukukura, Y.; Takumi, K.; Kamimura, K.; Shindo, T.; Kumagae, Y.; Tateyama, A.; Nakajo, M. Pancreatic Adenocarcinoma: Variability of Diffusion-weighted MR Imaging Findings. *Radiology* **2012**, *263* (3), 732–740.

(21) Nissan, N.; Golan, T.; Furman-Haran, E.; Apter, S.; Inbar, Y.; Ariche, A.; Bar-Zakay, B.; Goldes, Y.; Schvimer, M.; Grobgeld, D.; et al. Diffusion tensor magnetic resonance imaging of the pancreas. *PLoS One* **2014**, *9* (12), 1–19.

(22) Li, W.; Zhang, Z.; Nicolai, J.; Yang, G.-Y.; Omary, R. A.; Larson, A. C. Magnetization transfer MRI in pancreatic cancer xenograft models. *Magn. Reson. Med.* **2012**, *68* (4), 1291–1297.

(23) Li, W.; Zhang, Z.; Nicolai, J.; Yang, G. Y.; Omary, R. A.; Larson, A. C. Quantitative magnetization transfer MRI of desmoplasia in pancreatic ductal adenocarcinoma xenografts. *NMR Biomed.* **2013**, *26* (12), 1688–1695.

(24) Yin, T.; Peeters, R.; Feng, Y.; Liu, Y.; Yu, J.; Dymarkowski, S.; Himmelreich, U.; Oyen, R.; Ni, Y. Characterization of a rat orthotopic pancreatic head tumor model using three-dimensional and quantitative multi-parametric MRI. *NMR Biomed.* **2017**, *30* (2), 1–10.

(25) Vohra, R.; Park, J.; Wang, Y. N.; Gravelle, K.; Whang, S.; Hwang, J. H.; Lee, D. Evaluation of pancreatic tumor development in KPC mice using multi-parametric MRI. *Cancer Imaging* **2018**, *18* (1), 1–11.

(26) Perera, R. M.; Bardeesy, N. Pancreatic cancer metabolism: Breaking it down to build it back up. *Cancer Discov.* **2015**, *5* (12), 1247–1261.

(27) Wang, Z.; Chen, J. Q.; Liu, J. L.; Qin, X. G.; Huang, Y. FDG-PET in diagnosis, staging and prognosis of pancreatic carcinoma: A meta-analysis. *World J. Gastroenterol.* **2013**, *19* (29), 4808–4817.

(28) Warburg, O. Injuring of Respiration the Origin of Cancer Cells. *Science (80-. ).* **1956**, *123* (3191), 309–314.

(29) Golman, K.; Ardenkjær-Larsen, J. H.; Petersson, J. S.; Mansson, S.; Leunbach, I. Molecular imaging with endogenous substances. *Proc. Natl. Acad. Sci.* **2003**, *100* (18), 10435–10439.

(30) Kurhanewicz, J.; Vigneron, D. B.; Brindle, K.; Chekmenev, E. Y.; Comment, A.; Cunningham, C. H.; Deberardinis, R. J.; Green, G. G.; Leach, M. O.; Rajan, S. S.; et al. Analysis of cancer

metabolism by imaging hyperpolarized nuclei: prospects for translation to clinical research. *Neoplasia* **2011**, *13* (2), 81–97.

(31) Serrao, E. M.; Kettunen, M. I.; Rodrigues, T. B.; Dzien, P.; Wright, A. J.; Gopinathan, A.; Gallagher, F. A.; Lewis, D. Y.; Frese, K. K.; Almeida, J.; et al. MRI with hyperpolarised [1- $^{13}$C]pyruvate detects advanced pancreatic preneoplasia prior to invasive disease in a mouse model. *Gut* **2016**, *65* (3), 465–475.

(32) Stødkilde-Jørgensen, H.; Laustsen, C.; Hansen, E. S. S.; Schulte, R.; Ardenkjaer-Larsen, J. H.; Comment, A.; Frøkiær, J.; Ringgaard, S.; Bertelsen, L. B.; Ladekarl, M.; et al. Pilot Study Experiences With Hyperpolarized [1- 13 C]pyruvate MRI in Pancreatic Cancer Patients. *J. Magn. Reson. Imaging* **2019**, jmri.26888.

(33) Dutta, P.; Perez, M. R.; Lee, J.; Kang, Y.; Pratt, M.; Salzillo, T. C.; Weygand, J.; Zacharias, N. M.; Gammon, S. T.; Koay, E. J.; et al. Combining Hyperpolarized Real-Time Metabolic Imaging and NMR Spectroscopy To Identify Metabolic Biomarkers in Pancreatic Cancer. *J. Proteome Res.* **2019**, *18* (7), 2826–2834.

(34) Hingorani, S. R.; Wang, L.; Multani, A. S.; Combs, C.; Deramaudt, T. B.; Hruban, R. H.; Rustgi, A. K.; Chang, S.; Tuveson, D. A. Trp53R172H and KrasG12D cooperate to promote chromosomal instability and widely metastatic pancreatic ductal adenocarcinoma in mice. *Cancer Cell* **2005**, *7* (5), 469–483.

(35) Hruban, R. H.; Adsay, N. V.; Albores-Saavedra, J.; Anver, M. R.; Biankin, A. V; Boivin, G. P.; Furth, E. E.; Furukawa, T.; Klein, A.; Klimstra, D. S.; et al. Pathology of Genetically Engineered Mouse Models of Pancreatic Exocrine Cancer: Consensus Report and Recommendations. *Cancer Res.* **2006**, *66* (1), 95–106.

(36) Corbett, T. H.; Wilkoff, L. J.; Griswold, D. P.; Schabel, F. M.; Peckham, J. C.; Roberts, B. J.; Leopold, W. R. Induction and Chemotherapeutic Response of Two Transplantable Ductal Adenocarcinomas of the Pancreas in C57BL/6 Mice. *Cancer Res.* **1984**, *44*, 717–726.

(37) Upadhrasta, S.; Elias, H.; Patel, K.; Zheng, L. Managing cardiotoxicity associated with immune checkpoint inhibitors. *Chronic Dis. Transl. Med.* **2019**, *5* (1), 6–14.

(38) Grimm, J.; Potthast, A.; Wunder, A.; Moore, A. Magnetic resonance imaging of the pancreas and pancreatic tumors in a mouse orthotopic model of human cancer. *Int. J. Cancer* **2003**, *106* (5), 806–811.

(39) Jiang, Y. J.; Lee, C. L.; Wang, Q.; Zhou, Z. W.; Yang, F.; Jin, C.; Fu, D. L. Establishment of an orthotopic pancreatic cancer mouse model: Cells suspended and injected in Matrigel. *World J. Gastroenterol.* **2014**, *20* (28), 9476–9485.

(40) Carrière, C.; Young, A. L.; Gunn, J. R.; Longnecker, D. S.; Korc, M. Acute pancreatitis markedly accelerates pancreatic cancer progression in mice expressing oncogenic Kras. *Biochem. Biophys. Res. Commun.* **2009**, *382* (3), 561–565.

(41) Solomon, E.; Shemesh, N.; Frydman, L. Diffusion weighted MRI by spatiotemporal encoding: Analytical description and in vivo validations. *J. Magn. Reson.* **2013**, *232*, 76–86.

(42) Bao, Q.; Liberman, G.; Solomon, E.; Frydman, L. High-resolution diffusion MRI studies of development in pregnant mice visualized by novel spatiotemporal encoding schemes. *NMR Biomed. NMR Biomed.* **2020**, *33,* e4208.

(43) Bao, Q.; Ma, L.; Liberman, G.; Solomon, E.; Martinho, R. P.; Frydman, L. Dynamic T 2 mapping by multi-spin-echo spatiotemporal encoding. *Magn. Reson. Med.* **2020**, *84*, 895–907.

(44) Le Bihan, D.; Poupon, C.; Amadon, A.; Lethimonnier, F. Artifacts and pitfalls in diffusion MRI. *J. Magn. Reson. Imaging* **2006**, *24* (3), 478–488.

(45) Tal, A.; Frydman, L. Single-scan multidimensional magnetic resonance. *Prog. Nucl. Magn. Reson. Spectrosc.* **2010**, *57* (3), 241–292.

(46) Zhao, L.; Mulkern, R.; Tseng, C. H.; Williamson, D.; Patz, S.; Kraft, R.; Walsworth, R. L.; Jolesz, F. A.; Albert, M. S. Gradient-echo imaging considerations for hyperpolarized 129 Xe MR. *J. Magn. Reson. - Ser. B* **1996**, *113* (2), 179–183.

(47) Wang, L.; Gaddam, S.; Wang, N.; Xie, Y.; Deng, Z.; Zhou, Z.; Fan, Z.; Jiang, T.; Christodoulou, A. G.; Han, F.; et al. Multiparametric Mapping Magnetic Resonance Imaging of Pancreatic Disease. *Front. Physiol.* **2020**, *11*, 1–12.

(48) Wang, M.; Gao, F.; Wang, X.; Liu, Y.; Ji, R.; Cang, L.; Shi, Y. Magnetic resonance elastography and T 1 mapping for early diagnosis and classification of chronic pancreatitis. *J. Magn. Reson. Imaging* **2018**, *48*, 837–845.

(49) D'Arceuil, H.; de Crespigny, A. The effects of brain tissue decomposition on diffusion tensor imaging and tractography. *Neuroimage* **2007**, *36* (1), 64–68.

(50) Shepherd, T. M.; Thelwall, P. E.; Stanisz, G. J.; Blackband, S. J. Aldehyde fixative solutions alter the water relaxation and diffusion properties of nervous tissue. *Magn. Reson. Med.* **2009**, *62* (1), 26–34.

(51) Kartalis, N.; Manikis, G. C.; Loizou, L.; Albiin, N.; Zöllner, F. G.; Del Chiaro, M.; Marias, K.; Papanikolaou, N. Diffusion-weighted MR imaging of pancreatic cancer: A comparison of mono-exponential, bi-exponential and non-Gaussian kurtosis models. *Eur. J. Radiol. Open* **2016**, *3*, 79–85.

(52) Guglielmetti, C.; Najac, C.; Didonna, A.; Van Der Linden, A.; Ronen, S. M.; Chaumeil, M. M. Hyperpolarized 13C MR metabolic imaging can detect neuroinflammation in vivo in a multiple sclerosis murine model. *Proc. Natl. Acad. Sci. U. S. A.* **2017**, *114* (33), E6982–E6991.

(53) Lewis, A. J. M.; Miller, J. J.; Lau, A. Z.; Curtis, M. K.; Rider, O. J.; Choudhury, R. P.; Neubauer, S.; Cunningham, C. H.; Carr, C. A.; Tyler, D. J. Noninvasive immunometabolic cardiac inflammation imaging using hyperpolarized magnetic resonance. *Circ. Res.* **2018**, *122* (8), 1084–1093.